Optics Letters

Quantum state tomography in a third-order integrated optical parametric oscillator

Roger Alfredo Kögler,[1,*] Gabriel Couto Rickli,[1] Renato Ribeiro Domeneguetti,[2] Xingchen Ji,[3] Alexander L. Gaeta,[3,4] Michal Lipson,[3,4] Marcelo Martinelli,[1] and Paulo Nussenzveig[1]

[1]Instituto de Física, Universidade de São Paulo, Caixa Postal 66318, São Paulo, São Paulo 05315-970, Brazil
[2]Center for Macroscopic Quantum States (bigQ), Department of Physics, Technical University of Denmark, Fysikvej 307, Kgs. Lyngby DK-2800, Denmark
[3]Department of Electrical Engineering, Columbia University, New York, New York 10027, USA
[4]Department of Applied Physics and Applied Mathematics, Columbia University, New York, New York 10027, USA
*rogerkogler@alumni.usp.br

Received 9 February 2024; revised 4 April 2024; accepted 9 May 2024; posted 9 May 2024; published 29 May 2024

We measured the covariance matrix of the fields generated in an integrated third-order optical parametric oscillator operating above threshold. We observed up to (2.3 ± 0.3) dB of squeezing in amplitude difference and inferred (4.9 ± 0.7) dB of on-chip squeezing, while an excess of noise for the sum of conjugated quadratures hinders the entanglement. The degradation of amplitude correlations and state purity for increasing the pump power is consistent with the observed growth of the phase noise of the fields, showing the necessity of strategies for phase noise control aiming at entanglement generation in these systems.

https://doi.org/10.1364/OL.521339

Introduction. Novel photonic quantum technologies rely on integrated sources of nonclassical light, generating states that range from single photons to entangled states of bright fields. Optical parametric oscillators (OPOs) are widely employed for this purpose. The development of nanophotonics brought these devices into the microscale domain [1]. Nowadays, they represent a reliable source of entangled photons [2], being a building block to the realization of integrated quantum information protocols [3]. In the continuous variable domain, several important milestones were achieved, such as on-chip optical squeezing using second- ($\chi^{(2)}$) [4,5] and third-order ($\chi^{(3)}$) nonlinearities [6–11]. In particular, silicon photonics are of great interest due to their compatibility with the CMOS (complementary metal–oxide–semiconductor) fabrication process, enabling seamless integration of photonics and microelectronics in the same chip. Leveraged by its mature manufacturing industry, low loss waveguides are routinely fabricated, resulting in ultrahigh-quality factor optical micro-cavities [12].

Here, we present the full quantum tomography of the complete Gaussian states generated in an on-chip OPO for the first time. Aiming the observation of entanglement in those systems, theoretically predicted in Refs. [13,14], we reconstruct the four-mode covariance matrix of the output states with a resonator-assisted measurement technique [15,16]. Our results reveal unexpected effects resulting from the system dynamics in the studied operation regime. The present article is organized as follows: in the Materials and methods section, we describe our experimental system and the data analysis methods to reconstruct the covariance matrix from our measurements. The Results section shows the properties of the different states generated under different pump powers. Finally, we discuss the results and the limits in the production of quantum correlations in the Discussion and conclusion section.

Materials and methods. Our OPO consists of an on-chip silicon nitride microresonator on a silicon oxide substrate. Resonators with high-quality factors and strong light confinement boost intracavity powers and enhance third-order nonlinear interactions between resonant frequencies and the medium. The most relevant interactions in our system are self- and cross-phase modulations and the four-wave mixing (FWM), with the last being responsible for populating signal and idler modes. In the process, two photons of the pump mode are annihilated, and signal and idler photons are simultaneously generated, respecting energy conservation. Phase matching conditions, necessary for parametric gain around the optical pump, are guaranteed by anomalous group-velocity dispersion, which can be achieved by the combination of the material dispersion and our waveguide geometry (with 2630×730 nm^2 cross-section) [17]. Pairwise photon generation implies an intensity and amplitude correlation. Energy and momentum conservation leads to phase anti-correlation [13,14,18,19].

The micro-cavity is built with a closed-loop resonator with a free spectral range of 80 GHz, separated by a 250 nm gap from the bus waveguide. Its loaded and intrinsic quality factors are $Q_L = 2$ million and $Q_I = 16$ million, respectively. Therefore, the resonator is overcoupled for efficient intracavity light extraction, and up to 9.0 dB of squeezing is expected to be generated for an operation slightly above the optical threshold [19].

As schematically illustrated in Fig. 1, light from a 1560 nm diode laser (RIO ORION™) is amplified by an EDFA (erbium-doped fiber amplifier). The beam is sent through a filter cavity

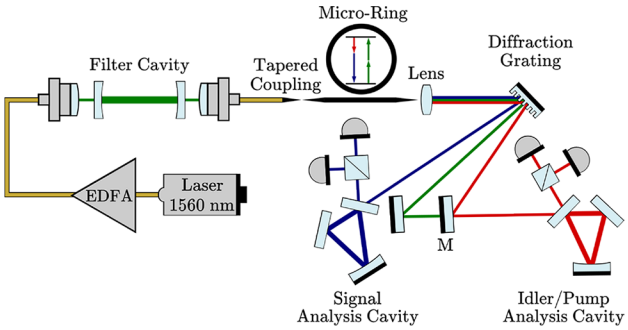

Fig. 1. Simplified scheme of the experimental setup.

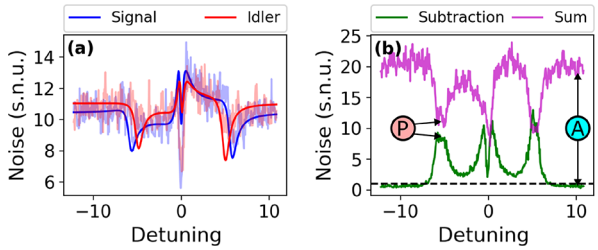

Fig. 2. (a) Power spectrum of the signal and idler fields. Straight lines are the fitted curves of Eq. (S10) of Supplement 1 to the faded acquired data in the background. (b) Noise for the sum and subtraction of the photocurrents. Two regions of the graphic that give us visual information on the amplitude (A circle) and phase (P circle) are indicated. s.n.u., shot noise units.

that reduces the noise close to a coherent state, as detailed in Sect. S2.A of Supplement 1. The resulting pump field is coupled into the chip using a tapered fiber, and a coupling efficiency of 70% is reached with the assistance of an inverse tapering design [20]. The guided field is evanescently coupled to the microresonator from the single bus waveguide, in an add-through configuration [21]. We tune the cavity into resonance by the thermo-optical effect [22] using an integrated micro-heater located over the resonator. Above the oscillation threshold of ~13.0 mW, bright signal (1544 nm) and idler (1578 nm) fields are produced, with an output in the range of a few mW. The output fields leave the chip and are collimated with an objective lens and spatially separated with a diffraction grating (600 grooves/mm and 13% losses).

After the separation, the signal and idler are reflected by individual analysis cavities, and the photocurrent generated by PIN photodiodes are further processed by a demodulation chain and registered on a computer for further analysis. Removal of mirror M allows the analysis of the pump field, and the use of a pair of detector allows for a permanent verification of the corresponding shot noise level by subtraction of the registered photocurrents. In this resonator-assisted detection scheme, we use the fact that the spectral analysis of the photocurrent $\hat{I}(t) = \int \hat{I}_\Omega e^{-i\Omega t} dt$ reveals, on the beatnote of combination of sidebands with the intense carrier field, the measurement of quadratures of these sidebands. Cavities will manipulate the phases of the involved fields, giving access to the distinct combination of quadratures that are projected into the amplitude fluctuations of the reflected beam [15]. Thus, we can reconstruct all the elements of the covariance matrix of the states [16]. We review the resonator-assisted detection scheme and the reconstruction of the single- and two-mode covariance matrices in Sect. S1 of Supplement 1.

The observables of the quadratures are related to the creation and annihilation operators of the upper and lower sideband modes: $\hat{p}_{\pm\Omega} = \hat{a}^\dagger_{\pm\Omega} + \hat{a}_{\pm\Omega}$ and $\hat{q}_{\pm\Omega} = i(\hat{a}^\dagger_{\pm\Omega} - \hat{a}_{\pm\Omega})$. These can be associated respectively with the amplitude and phase quadratures of the intense field. On the other hand, the detection process involving the spectral components (Ω) of the detectors' photocurrent will necessarily bring the information of the beat of the upper and lower sidebands with the intense mean field [16]. Thus, the description of the measurements can be conveniently expressed using a basis involving both symmetric and anti-symmetric combinations of these sidebands, defined as $\hat{p}_{\mathfrak{s}} = (\hat{p}_\Omega + \hat{p}_{-\Omega})/\sqrt{2}, \hat{p}_{\mathfrak{a}} = (\hat{p}_\Omega - \hat{p}_{-\Omega})/\sqrt{2}, \hat{q}_{\mathfrak{s}} = (\hat{q}_\Omega + \hat{q}_{-\Omega})/\sqrt{2}$ and $\hat{q}_{\mathfrak{a}} = (\hat{q}_\Omega - \hat{q}_{-\Omega})/\sqrt{2}$.

Therefore, the complete state of the Gaussian field involving the pair of sidebands of the converted fields can be associated with the covariance matrix [16]:

$$\mathbb{V} = \begin{bmatrix} \mathbb{V}_{\mathfrak{s}} & \mathbb{C}_{(\mathfrak{s},\mathfrak{a})} \\ \mathbb{C}^{\mathrm{T}}_{(\mathfrak{s},\mathfrak{a})} & \mathbb{V}_{\mathfrak{a}} \end{bmatrix}. \quad (1)$$

The sub-matrices are related to the sideband quadratures through $\mathbb{V}_{\mathfrak{s}} = \frac{1}{2}\left\langle \mathbf{x}_{\mathfrak{s}} \cdot \mathbf{x}^{\mathrm{T}}_{\mathfrak{s}} + \left(\mathbf{x}_{\mathfrak{s}} \cdot \mathbf{x}^{\mathrm{T}}_{\mathfrak{s}}\right)^{\mathrm{T}} \right\rangle$ and $\mathbb{V}_{\mathfrak{a}} = \frac{1}{2}\left\langle \mathbf{x}_{\mathfrak{a}} \cdot \mathbf{x}^{\mathrm{T}}_{\mathfrak{a}} + \left(\mathbf{x}_{\mathfrak{a}} \cdot \mathbf{x}^{\mathrm{T}}_{\mathfrak{a}}\right)^{\mathrm{T}} \right\rangle$, where we ordered the quadrature operators as $\mathbf{x}_j = \left[\hat{p}^{(s)}_j, \hat{q}^{(s)}_j, \hat{p}^{(i)}_j, \hat{q}^{(i)}_j\right]^{\mathrm{T}}$, $j = \{\mathfrak{s}, \mathfrak{a}\}$. The cross correlation matrix is given by $\mathbb{C}_{(\mathfrak{s},\mathfrak{a})} = \left\langle \mathbf{x}_{\mathfrak{s}} \cdot \mathbf{x}^{\mathrm{T}}_{\mathfrak{a}} \right\rangle$. Since the spectral component $\hat{I}(\Omega) \propto e^{-i\varphi}\hat{a}_\Omega + e^{i\varphi}\hat{a}^\dagger_{-\Omega}$ explicitly brings the contribution of the sidebands, with a phase φ of the carrier, the measurement of the noise power $\Delta^2 I^{(m)} = \langle \hat{I}^{(m)}(\Omega)\hat{I}^{(m)}(-\Omega)\rangle$ for signal and idler modes ($m = \{s, i\}$) and the cross correlation of the quadratures of the photocurrent $Re\{\langle \hat{I}^{(s)}(\Omega)\hat{I}^{(i)}(-\Omega)\rangle\}$ and $Im\{\langle \hat{I}^{(s)}(\Omega)\hat{I}^{(i)}(-\Omega)\rangle\}$ enable a full reconstruction of the covariance matrix $\mathbb{V}$ by the measurement of the photocurrents while scanning the analysis cavities.

Figure 2(a) shows one measurement of signal and idler photocurrents' noise power at 20 MHz, where the presented curve corresponds to the state with the optimum value of amplitude difference squeezing. Its covariance matrix elements are given in Tables S2 and S3 of Supplement 1. The corresponding frequency was selected in order to avoid excess of technical noise from the system and remain within the detection bandwidth. All data is corrected by the electronic noise and normalized by the shot noise level. Analysis cavity detuning is normalized by the idler cavity bandwidth of 4.74 MHz. As the cavity is swept around the resonance, one can see the variation on the noise level, indicating unequal quadrature noise. These curves carry part of the information necessary to reconstruct $\mathbb{V}_{\mathfrak{s}}$ and $\mathbb{V}_{\mathfrak{a}}$.

Providing that the measurements were taken synchronously as the cavities sweep around resonance ($\Delta = 0$), we can use the sum and subtraction of the photocurrents to verify quantum features in the EPR variables $\hat{p}_- = (\hat{p}^{(s)}_s - \hat{p}^{(i)}_s)/\sqrt{2}$ and $\hat{q}_+ = (\hat{q}^{(s)}_s + \hat{q}^{(i)}_s)/\sqrt{2}$, which can eventually witness entanglement if $\Delta^2 p_- + \Delta^2 q_+ < 2$ [23]. As shown in Fig. 2(b), far from resonance, amplitude difference squeezing is observed, as previously evidenced in similar systems operating above threshold [6,7], while the sum of the currents demonstrates strong anti-correlation in the amplitudes. On the other hand, strong correlations in phase quadratures are not present. This is an indication that we are generating highly mixed states at the chip output.

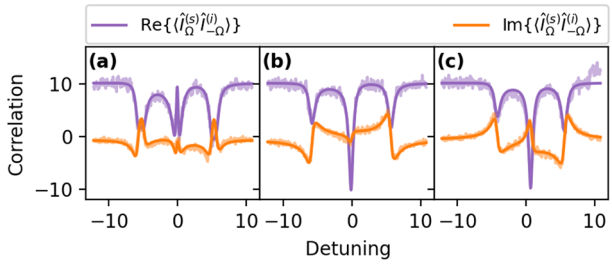

Fig. 3. Results from three iterations of the experiment. (a) Simultaneous sweeping of the signal and idler analysis cavities, using the same data leading to Fig. 2. (b) Highly detuned idler cavity while sweeping the signal cavity. (c) Highly detuned signal cavity while sweeping the idler cavity. The fitted curves are given by Eqs. (S15) and (S16) of Supplement 1.

Although we retrieve some elements of the covariance matrix from the single- and two-mode power spectra in the sum and subtraction subspaces, the complete reconstruction of the covariance matrix requires access to the cross correlations in $\mathbb{C}_{(s,a)}$. The full tomography of the quantum state is performed through three sequential measurements of the experiment, which are treated in detail in Sect. S1 of Supplement 1. First, the analysis cavities are swept around resonance synchronously, accessing the correlation of on-phase quadratures of the fields. The cross-quadrature correlations are accessed by asynchronous measurements maintaining one cavity far from resonance while sweeping the other. Figure 3 shows the data and the fittings of the correlation functions for the same example and conditions presented in Fig. 2.

Results. Once the measurement procedure and the analysis method for the covariance matrix reconstruction were well defined, we carried out a sequence of experiments varying the pump power, and the final results were evaluated considering the total measurement efficiency of 61% (11% from the output coupling into free space, 13% from the diffraction grating, 4% from the mismatch with the analysis cavities, 9% from optical components, and 90% from a detector's quantum efficiency), giving the on-chip state of the field.

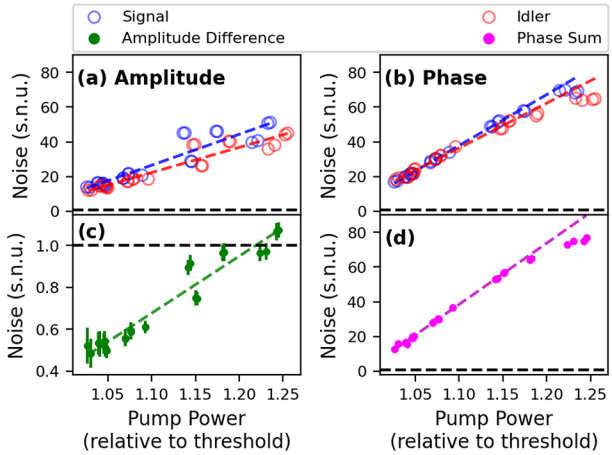

Fig. 4. (a) Amplitude and (b) phase quadrature noise as a function of the pump power. (c) Amplitude difference squeezing. (d) Phase quadrature sum noise. Dashed lines indicate the shot noise level. Error bars in (a), (b), and (d) are buried under the points due to the large scales. s.n.u., shot noise units.

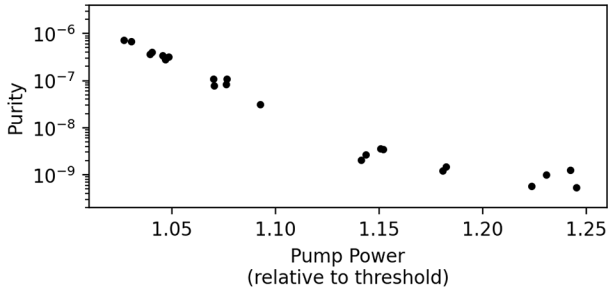

Fig. 5. Purity of the measured states, Eq. (S25) of Supplement 1. Error bars are buried under the points.

Figure 4 presents the behavior of the quadrature's noise for distinct pump powers (normalized to the 13 mW threshold). There is a dramatic increase of the noise power, shown in Figs. 4(a) and 4(b). As a consequence, any imbalance between the beams caused by the dynamics of the system will lead to the degradation of correlations. This can be seen as a degradation of squeezing in amplitude difference, as shown in Fig. 4(c). This result is in contrast to what is observed in $\chi^{(2)}$ [24,25] and $\chi^{(3)}$ [26] OPOs, where a constant degree of squeezing is observed for an increasing pumping power. One reason for that is the mixture of phase and amplitude quadratures due to the phase modulations induced by the dynamics of the third-order OPO [13,27] and the generation of additional sideband modes [28] as the intracavity power builds up. Regarding the sum of the quadratures, correlations are not enough to compensate the excess noise, specially at higher pump powers [Fig. 4(d)].

The purity of the states is readily accessible through the determinant of the covariance matrix [29], as shown in Eq. (S25) of Supplement 1. The increasing noise in the quadratures and the degradation of correlations affect the purity of the system, which decreases drastically as we move away from the oscillation threshold, as shown in Fig. 5. As already stated, no entanglement was expected from the states due to the high phase sum noise. We thoroughly checked this through the application of the PPT criterion [30] between all possible partitions of the system (Fig. S13 of Supplement 1). Intrinsic parametric processes [13,27] will not degrade the purity of the system, and entanglement should yet be noticed from PPT, in this sense a more efficient method than the direct measurement of the EPR-like quadratures [23].

Therefore, the source of this loss of purity must lie somewhere else. The remaining noise of the pump (≈8 dB as seen in Sec. 2.A of Supplement 1) could not justify the strong noise in the outputs. As a primordial diagnostic of our system, we compute the behavior of the pump noise with the intensity by operating the integrated OPO below the oscillation threshold. We coupled the pump field in the idler analysis cavity to measure its power spectrum. The amplitude and phase noise for increasing values of the pump field are shown in Fig. 6. The approximately linear behavior of the fast increasing pump phase noise with a pump power is in agreement with previous evidence of photon scattering caused by phonons in $\chi^{(2)}$ crystals [25]. Moreover, previous investigations of the influence of thermal noise in light propagating in waveguides [31] and microresonators [32] are compatible with a thermorefractive origin. The mitigation of the excessive noise may then be achieved by cooling the system [33]. This observation suggests a path for future investigations toward the

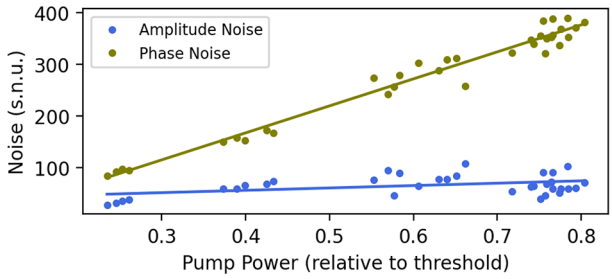

Fig. 6. Evolution of the amplitude and phase noise of the pump field for the OPO operating below threshold as a function of its power.

generation of entangled states. We expect to study the impact of the temperature on the quantum dynamics of the on-chip OPO above threshold.

Discussion and conclusion. The reconstruction of the covariance matrices of the intense signal and idler beams generated in an integrated $\chi^{(3)}$ OPO operating above the oscillation threshold is a powerful diagnostic tool to understand the limitations for entangled field generation above the oscillation threshold in these systems.

Using cavity-assisted detection, we were able to perform the tomography of the four-mode state described by the upper and lower sidebands of the signal and idler modes. Strong amplitude correlations, beating the standard quantum level, were directly measured, and up to 2.3 ± 0.3 dB of raw squeezing was observed, as shown in Fig. 4(c). Correcting for losses, we infer a total of 4.9 ± 0.7 dB of on-chip optical squeezing. This result is against the expected 9.0 dB of squeezing, given the OPO properties of the study. We attribute this to the unforeseen on-chip mechanisms of thermal origin and the contamination of the phase noise in the amplitude quadrature due to distortions of the noise ellipse induced by Kerr effect phase modulations [13,27].

Observing entanglement remains a challenge, as demonstrated by current results. The four-mode state is highly mixed with a large excess of noise in the phase sum quadrature. Moreover, for stronger pump powers, the noise present in the fields' quadratures increases, and amplitude correlations are degraded as the dynamics of the system unbalance the signal and idler.

The noise of the pump, below the oscillation threshold, is consistent with an excess noise of thermal origin observed in [25,31,32]. Hence, probing the temperature effects on the integrated OPO is an experimental route that may enable the measurement of entanglement in the future work. Our results shine light on one of the bottlenecks hindering the deterministic generation of entangled states with on-chip silicon-based OPOs above threshold.

Funding. Fundação de Amparo à Pesquisa do Estado de São Paulo (2013/26757 – 0, 2015/18834 – 0, 2021/04829 – 6); Coordenação de Aperfeiçoamento de Pessoal de Nível Superior (001).

Disclosures. The authors declare no conflicts of interest.

Data availability. Data underlying the results presented in this paper are not publicly available at this time but may be obtained from the authors upon reasonable request.

Supplemental document. See Supplement 1 for supporting content.

REFERENCES

1. T. Kippenberg, S. Spillane, and K. Vahala, Phys. Rev. Lett. **93**, 083904 (2004).
2. Z. Yin, K. Sugiura, H. Takashima, *et al.*, Opt. Express **29**, 4821 (2021).
3. D. Llewellyn, Y. Ding, I. I. Faruque, *et al.*, Nat. Phys. **16**, 148 (2020).
4. F. Mondain, T. Lunghi, A. Zavatta, *et al.*, Photonics Res. **7**, A36 (2019).
5. P.-K. Chen, I. Briggs, S. Hou, *et al.*, Opt. Lett. **47**, 1506 (2022).
6. A. Dutt, K. Luke, S. Manipatruni, *et al.*, Phys. Rev. Appl. **3**, 044005 (2015).
7. A. Dutt, S. Miller, K. Luke, *et al.*, Opt. Lett. **41**, 223 (2016).
8. V. D. Vaidya, B. Morrison, L. Helt, *et al.*, Sci. Adv. **6**, eaba9186 (2020).
9. Y. Zhao, Y. Okawachi, J. K. Jang, *et al.*, Phys. Rev. Lett. **124**, 193601 (2020).
10. Y. Zhang, M. Menotti, K. Tan, *et al.*, Nat. Commun. **12**, 2233 (2021).
11. M. Jahanbozorgi, Z. Yang, S. Sun, *et al.*, Optica **10**, 1100 (2023).
12. Y. Xuan, Y. Liu, L. T. Varghese, *et al.*, Optica **3**, 1171 (2016).
13. C. González-Arciniegas, N. Treps, and P. Nussenzveig, Opt. Lett. **42**, 4865 (2017).
14. A. Bensemhoun, C. Gonzalez-Arciniegas, O. Pfister, *et al.*, Phys. Lett. A **493**, 129272 (2024).
15. A. S. Villar, Am. J. Phys. **76**, 922 (2008).
16. F. A. Barbosa, A. S. Coelho, K. N. Cassemiro, *et al.*, Phys. Rev. A **88**, 052113 (2013).
17. A. C. Turner, C. Manolatou, B. S. Schmidt, *et al.*, Opt. Express **14**, 4357 (2006).
18. A. B. Matsko, A. A. Savchenkov, D. Strekalov, *et al.*, Phys. Rev. A **71**, 033804 (2005).
19. Y. K. Chembo, Phys. Rev. A **93**, 033820 (2016).
20. J. Cardenas, C. B. Poitras, K. Luke, *et al.*, IEEE Photonics Technol. Lett. **26**, 2380 (2014).
21. A. Yariv, Electron. Lett. **36**, 321 (2000).
22. A. R. Zanatta and I. B. Gallo, Appl. Phys. Express **6**, 042402 (2013).
23. L.-M. Duan, G. Giedke, J. I. Cirac, *et al.*, Phys. Rev. Lett. **84**, 2722 (2000).
24. J. Jing, S. Feng, R. Bloomer, *et al.*, Phys. Rev. A **74**, 041804 (2006).
25. J. César, A. Coelho, K. Cassemiro, *et al.*, Phys. Rev. A **79**, 063816 (2009).
26. A. M. Guerrero, P. Nussenzveig, M. Martinelli, *et al.*, Phys. Rev. Lett. **125**, 083601 (2020).
27. G. Ferrini, I. Fsaifes, T. Labidi, *et al.*, J. Opt. Soc. Am. B **31**, 1627 (2014).
28. A. L. Gaeta, M. Lipson, and T. J. Kippenberg, Nat. Photonics **13**, 158 (2019).
29. M. G. Paris, F. Illuminati, A. Serafini, *et al.*, Phys. Rev. A **68**, 012314 (2003).
30. R. Simon, Phys. Rev. Lett. **84**, 2726 (2000).
31. N. Le Thomas, A. Dhakal, A. Raza, *et al.*, Optica **5**, 328 (2018).
32. G. Huang, E. Lucas, J. Liu, *et al.*, Phys. Rev. A **99**, 061801 (2019).
33. R. Cernansky and A. Politi, APL Photonics **5**, 101303 (2020).